Modelling metasurface patterned anode for enhanced performance of solid oxide electrolyser.

KURUSHINA, V., HOSSAIN, M., HASBI, S., SOMAN, A., CAI, Q., HORRI, B.A. and FAISAL, N.H.

2025

Journal of Power Sources 648 (2025) 237436

Contents lists available at ScienceDirect

Journal of Power Sources

journal homepage: www.elsevier.com/locate/jpowsour

Modelling metasurface patterned anode for enhanced performance of solid oxide electrolyser

Victoria Kurushina [a,b,*], Mamdud Hossain [a,**], Syafawati Hasbi [a], Ajith Soman [c], Anil Prathuru [a], Qiong Cai [c], Bahman Amini Horri [c], Nadimul Haque Faisal [a,***]

[a] School of Computing, Engineering and Technology, Robert Gordon University, Aberdeen, AB10 7GJ, UK
[b] Laboratory of Vibration & Hydrodynamics Modelling, Industrial University of Tyumen, Tyumen, 625 000, Russia
[c] Department of Chemical & Process Engineering, University of Surrey, Guildford, GU2 7XH, UK

HIGHLIGHTS

- Tubular solid oxide electrolysis (SOE) cell investigated with the metallic support.
- Introduced a metasurface-patterned anode structure for enhanced performance.
- Simulations are performed for the 1/16th sector model of the short tubular cell.
- Current density evaluated for four types of the porous anode metasurface.
- Net-structure metasurface of the porous anode found to be the most efficient by 8.5 %.

GRAPHICAL ABSTRACT

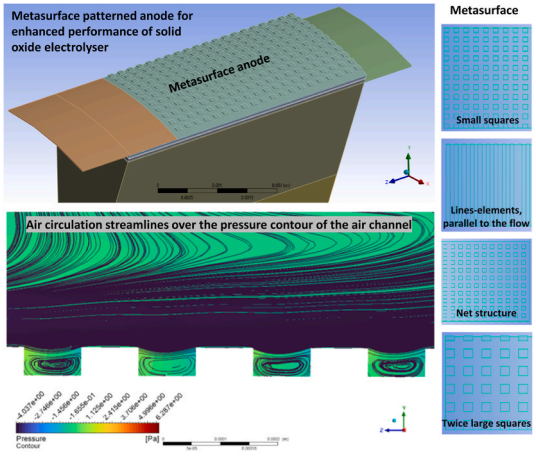

ARTICLE INFO

Keywords:
Solid oxide electrolysis
High temperature electrolysis
Metasurface
Modelling

ABSTRACT

Solid oxide electrolysers (SOE) are a promising type of technology of hydrogen production with the potential to be a part of the sustainable future of the energy sector. Advantageous efficiency of these devices is coming from the combined use of the heat and electrical energy. The current research proposes to improve the electrical efficiency of solid oxide electrolysers by fabricating a metasurface upon the standard porous anode layer of the electrolysis cell. The study considers the tubular cell design with the thick metallic support and several types of meta-elements, including squared shapes, lines parallel to the air flow and a net-structured surface.

* Corresponding author. School of Computing, Engineering and Technology, Robert Gordon University, Aberdeen, AB10 7GJ, UK.
** Corresponding author.
*** Corresponding author.
E-mail addresses: v.kurushina@outlook.com (V. Kurushina), m.hossain@rgu.ac.uk (M. Hossain), n.h.faisal@rgu.ac.uk (N.H. Faisal).

https://doi.org/10.1016/j.jpowsour.2025.237436
Received 4 November 2024; Received in revised form 2 May 2025; Accepted 20 May 2025
Available online 24 May 2025

Computational fluid dynamics (CFD) analysis is performed for the 1/16 sector model of the tubular cell in parallel flow conditions to evaluate current density characteristics of the considered metasurfaces. As a result of this study, the net-structured metasurface is found to increase the current density by 8.5 %.

1. Introduction

On the landscape of hydrogen production technologies, solid oxide high-temperature electrolysis is both an ecologically friendly method of water splitting and also a way to utilise the waste heat and electricity, with both stable and periodical availability [1,2]. Solid oxide electrolysis cells (SOECs) have all the potential to become a critical technology in the sustainable future of the energy sector, due to their high efficiency [3,4], multiple integration possibilities, and use of solid materials for functional layers. Applications of solid oxide electrolysers already include the onshore and offshore energy infrastructure [5], transport (aviation, submarines, buses) [6], space (in-orbit and deep space) [7–10], with the potential to be a part of the further space exploration activities [11–16].

Solid oxide electrolysis (SOE) is one of the stepping stones of building both the hydrogen economy and the Net Zero [17] vision of the future. In this strategic vision, hydrogen becomes a widely used clean energy carrier, fully replacing or accompanying fossil fuels, the process which implies growth and development of new production, transportation, storage and utilization facilities [18–20]. The SOE production technology belongs to the green hydrogen direction of development in the hydrogen economy, where the hydrogen production can be integrated with renewable energy systems. Importance of the SOE in the economy may grow, as the technology matures [4], building on its strengths, including exceptional purity of hydrogen and oxygen produced, high efficiency and controllability of reaction rates with temperature, compatibility with a wide range of systems, possibility to consume waste heats and suitability for an intermittent operation. The list of current challenges for the technology includes high costs, material degradation problem, choice of materials, making the cell fabrication process more environmentally friendly, and some lack of commercialization and manufacturing innovation.

Research on solid oxide electrolysers dates back to as early as 1940s ([21,22] and mainly focuses on experimentally found properties of ceramic materials at a high temperature, - conditions, when the electrochemical reaction begins. The studies of material properties, fabrication and use of SOEC continued in later years [23–30] and were expanded towards other materials used as electrolysers and also towards the concept of co-electrolysis of water and carbon dioxide [31–33]. Experimental research of that time explored many available solid oxides, one-by-one, to map their properties, including elements of nickel, lanthanum, cobalt, zirconium, yttrium, which are currently in use for the cell fabrication.

Simulation approaches for solid oxide electrolysis developed around the mass and energy conservation equations [34], reaction kinetics [35] and eventually branched into 0D, 1D, 2D, 3D modelling approaches [36]. The 3D simulations are used for the detailed examination of specific problems, and the related time costs lead to a trade off with the accuracy. 0D models work with the largest number of empirical and semi-empirical expressions, assumptions and process simplifications. These models are applicable, where effects of the geometry do not have to be evaluated. Kupecki et al. [36] recommend the 1D and 2D models as an extension of 0D models, to take into account boundary conditions and the geometry.

At the present time, development of solid oxide electrolysers widely uses capabilities and accumulated research experience of Multiphysics models ([37]; [38–40]) and computational fluid dynamics (CFD) approach [41–44], applied of the cell level. During the past twenty years, CFD method has integrated the solution of the Navier-Stokes system with the electro-chemistry models, energy transfer, species transport, - all components of modelling that are essential for a detailed consideration of electrolysers. CFD is used in several directions of the SOEC development: (a) assessing performance for a new cell design [45], (b) investigating transient operating conditions [46]; (c) finding optimal operating conditions [47], (d) evaluating long- and short-term impacts of structural changes (including the electrode degradation) [48], (e) forecasting the lifetime of a cell or a stack, (f) investigating the design, amount and direction of flow channels [49–52], (g) investigating design of the current collection, (h) studying the optimal support types for the cell, (i) evaluating performance of a stack ([53]; [54]), a plant [55] or a larger integrated system [56].

Analysis of the CFD studies in the literature suggests that there is still a room for the design improvement of available SOECs in terms of changes to the structural geometry and the general layout of the cell. Similar to the modelling approaches [38], structural changes may be distinguished by the level, from nanoscale to macroscale advancements. Engineered changes to the microscale structure, relevant to the thin functional layers of solid oxide electrolysers, belong to the area of metamaterials. Metamaterials already play a pivotal role on the pathway to sustainable energy production in Earth environment and in harsh conditions of other celestial bodies. Metamaterials and metasurfaces offer unprecedented opportunities to enhance efficiency and scalability across various energy sectors, including hydrogen production. Metamaterial-based solutions already improve performance of solar energy harvesting with ultra-efficient photovoltaic cells, harvesting mechanical energy [57], batteries and thermal emitters. The opportunities come with the challenge of the precise fabrication and large-scale manufacturing of 3D metasurfaces, as discussed in Ref. [58]. Here, the thermal sprayed and plasma-sprayed thin coatings deposited on the substrate are studied experimentally, with potential applications for a range of opto-electronic, electromagnetic and electrochemically active devices.

In [59], fabrication of pillar-structured Ni-YSZ electrode is considered for the solid oxide electrochemical reactor in the fuel cell and electrolysis modes. Cylindrical pillars are manufactured using 3D printing technology in 30, 60 and 90 layers of the material, identical with the electrode. The paper reports the performance enhancement by a factor of 3 in the steam electrolysis mode, when the surface with cylindrical pillars consists of all the functional layers for a planar cell design. The research focused on temperatures of 700 °C–800 °C. The work is based on the previous advancements in the 3D printing technology for cylindrical structure on the electrode layers [60,61].

CFD analysis for the conical, cylindrical pillars and a plain cell is performed in Ref. [62] for the closely (63 μm apart) positioned elements. Here, metasurface is formed by all the functional layers, including the anode, electrolyte and cathode. The paper used COMSOL software and obtained 14 % improvement in the current density for the electrolysis mode. Cylindrical pillars were found more efficient as well. The study also explored the dependence between the height and the diameter of the metasurface elements and recommended to apply increased height with an increased diameter together, and vice versa.

Following these works [58,59,62] and the design proposed in Ref. [2], the current research is investigating the potential of applying metasurface elements at the porous anode layer in the tubular solid oxide steam electrolyser, while using alternative configurations. In this setting, the metastructure of the porous anode layer comes in the direct contact with the air, surrounding the tubular cell. Following the increase in the electrochemically active area, achieved for each subsequent layer of a tubular cell design, the expectation from implementing the metasurface is in increasing the active area of the anode even further and,

therefore, in enhancing the overall electrical efficiency of the electrolysis. The current study employs the CFD approach to evaluate the current density characteristics of the SOEC with and without the metasurface.

2. Methodology

2.1. Model set-up

The considered system represents the sector of a tubular SOEC model, which is 1/16 of the full cell design, cut along the length of the cell. The general view of the sector model is given in Fig. 1. Short 5 mm long cell design is considered, and the principal sizes are summarized in Table 1. The total thickness of the cell wall is 2.332 mm, including the thick supporting titanium substrate layer. Design porosity of 30 % is assumed for simulations for all layers of the cell. While a dense electrolyte is needed for high ionic conductivity, some controlled porosity can relieve thermal stress and cracking, enhancing the overall durability of the SOE for either fabrication method. A well-designed porosity ensures that reactants and products move efficiently, reducing concentration polarization losses. It can also help maintain a balance between ionic conductivity and gas diffusion. The electrolyte projected area is 1.02855e-5 m^2. The open circuit voltage (OCV) is set to 1.1 V in this work for majority of the simulations. The current density is reported at the interface between the cathode and the porous cathode layer, because the electrochemical reactions primarily occur at this triple-phase boundary (TPB), where the electron-conducting cathode, ion-conducting electrolyte, and gaseous reactants meet. Calculations are performed in this study with the computational fluid dynamics (CFD) approach for a steady state, for 1 atmospheric pressure in the internal fluid channel and for the parallel flow conditions in the channels. The mesh model is shown in Fig. 1(a), while functional layers and a belt-like current collector are detailed in Fig. 1(b). Inlets and outlets of the two fluid channels are illustrated in Fig. 1(c), all other boundaries of the fluid dynamics model are assumed to be walls. Mass flow rates are 1e-6 kg/s for the air inlet and 1e-5 kg/s for the steam inlet. Simulations also assume 10 % portion of hydrogen and 90 % portion of steam on the steam inlet. Anode exchange current density is assumed to be 2000 A/m^2, and cathode exchange current density is set to 7500 A/m^2, following the research in Ref. [49]. The operating temperature considered is 1073 K (800 °C).

Materials used for layers of the model are given in Table 2, with the final properties listed in Table 3 for the three layers, composed of the material mixture. Substrate or metal support is composed of titanium (Ti), anode/cathode current collector – of silver (Ag), cathode – of nickel oxide (NiO) and gadolinia-doped ceria (GDC), electrolyte – of gadolinia-doped ceria (GDC) and yttria-stabilized zirconia (YSZ), anode – of gadolinia-doped ceria (GDC) and lanthanum strontium cobalt ferrite (LSCF). Metasurface elements, considered further, are deposited upon the porous anode layer and consist of the same material, as this layer. Sample of the model geometry with the metasurface applied to the porous anode is shown in Fig. 2. CFD model in ANSYS Fluent for the electrolysis with the resolved electrolyte interprets the substrate layer and the thin functional layers as a fluid zone with a porous medium, current collectors are solid bodies, and fluid channels are plain fluid zones.

2.2. Governing equations

The algorithm in ANSYS Fluent combines the solution of the Navier-Stokes fluid dynamics equations, with the species transport, chemical reactions model, current conservation, charge transport, energy equation, which are all essential in order to model the electrolysis process with sufficient details [49,63]. In the current simulations, the resolved electrolyte model is applied, and the 3D numerical model of the cell is created.

The continuity equation is defined for this process as follows:

$$\nabla \cdot (\rho U) = S_m, \tag{1}$$

where ρ is the fluid density, S_m is the source term, which is 0, except for the triple phase boundary (TPB) with $S_m = \sum_i S_{m,i}$. Equation (1) applies for three dimensions and for all materials and phases in the flow.

The momentum equation is used with the laminar flow viscosity:

$$\nabla \cdot (\rho UU) = -\nabla \mathrm{P} + \nabla \cdot (\mu \nabla U) + S_d, \tag{2}$$

where P stands for the fluid pressure, μ is dynamic viscosity, and the source term $S_d = 0$ applies to the fluid channels, while $S_d = -\frac{\mu}{k}U$ corresponds to the TPBs and diffusion layers, and k is the kinetic energy.

The energy balance equation includes the heat capacity C_p, absolute temperature variable T and the source term S_T:

$$\nabla \cdot \left(\rho C_p U T\right) = -\nabla (k \nabla T) + S_T, \tag{3}$$

The source term in Eq. (3) is $S_T = \frac{j^2}{\sigma}$ for the diffusion layer, electrodes, metal support and interconnects, and $S_T = \frac{j^2}{\sigma} + j\left(\eta_{act} + \frac{T\Delta S}{2F}\right)$ is used for TPBs. Here, j is the volumetric current density, η_{act} is the activation polarization, F is the Faraday constant, S is the value of entropy, σ stands for the electric conductivity.

The species transport equation defines motion and diffusion of the i th component in the mixture:

$$\nabla \cdot (\rho U Y_i) = -\nabla \cdot J_i + S_{m,i}, \tag{4}$$

where the source terms are $S_{m,i} = 0$ everywhere, except $S_{m,i} = \frac{j}{n_e F} M_i$ for TPBs, and Y_i is the molar fraction of the i th species. Here, the total number of species in the mixture is N.

The charge transport equation establishes the link between the input current and voltage and the potential Φ across the cell, which reads as:

$$-\nabla \cdot (\rho \nabla \Phi) = S_\phi, \tag{5}$$

where the source term is $S_\phi = 0$ for all layers, except TPBs, where $S_\phi = j$.

The current conservation equation applies to the electrolysis cell model, in order to represent the balance in the volumetric current density on the anode j_{an} and the cathode j_{cat} sides:

$$\int_{anode} j_{an} dV = \int_{cathode} j_{cat} dV, \tag{6}$$

where V is the volume.

The Fick's law is a simple diffusion model and establishes the dependence of the mass diffusion flux J_i from temperature T and size of the spatial grid ∇Y_i:

$$J_i = -\rho D_{m,i}^{eff} \nabla Y_i - D_{T,i} \frac{\nabla T}{T}, \tag{7}$$

where $D_{T,i}$ is defined as the thermal diffusion coefficient of the i th component in the transported mixture, $D_{m,i}^{eff}$ is the effective mass diffusion coefficient for the i th component.

The Stefan-Maxwell equations used for simulations extend the Fick's law for N number of components in the mixture:

$$\sum_{j=1, j\neq i}^{N} \frac{Y_i Y_j}{D_{ij}} \left(\frac{J_i}{\rho_i} - \frac{J_j}{\rho_j}\right) = \nabla Y_i - \frac{\nabla T}{T} \sum_{j=1, j\neq i}^{N} \frac{Y_i Y_j}{D_{ij}} \left(\frac{D_{T,j}}{\rho_j} - \frac{D_{T,i}}{\rho_i}\right), \tag{8}$$

where D_{ij} is the binary diffusion coefficient used to approximate the equation. Here, the pressure diffusion is neglected, and the external force is assumed equal to all species.

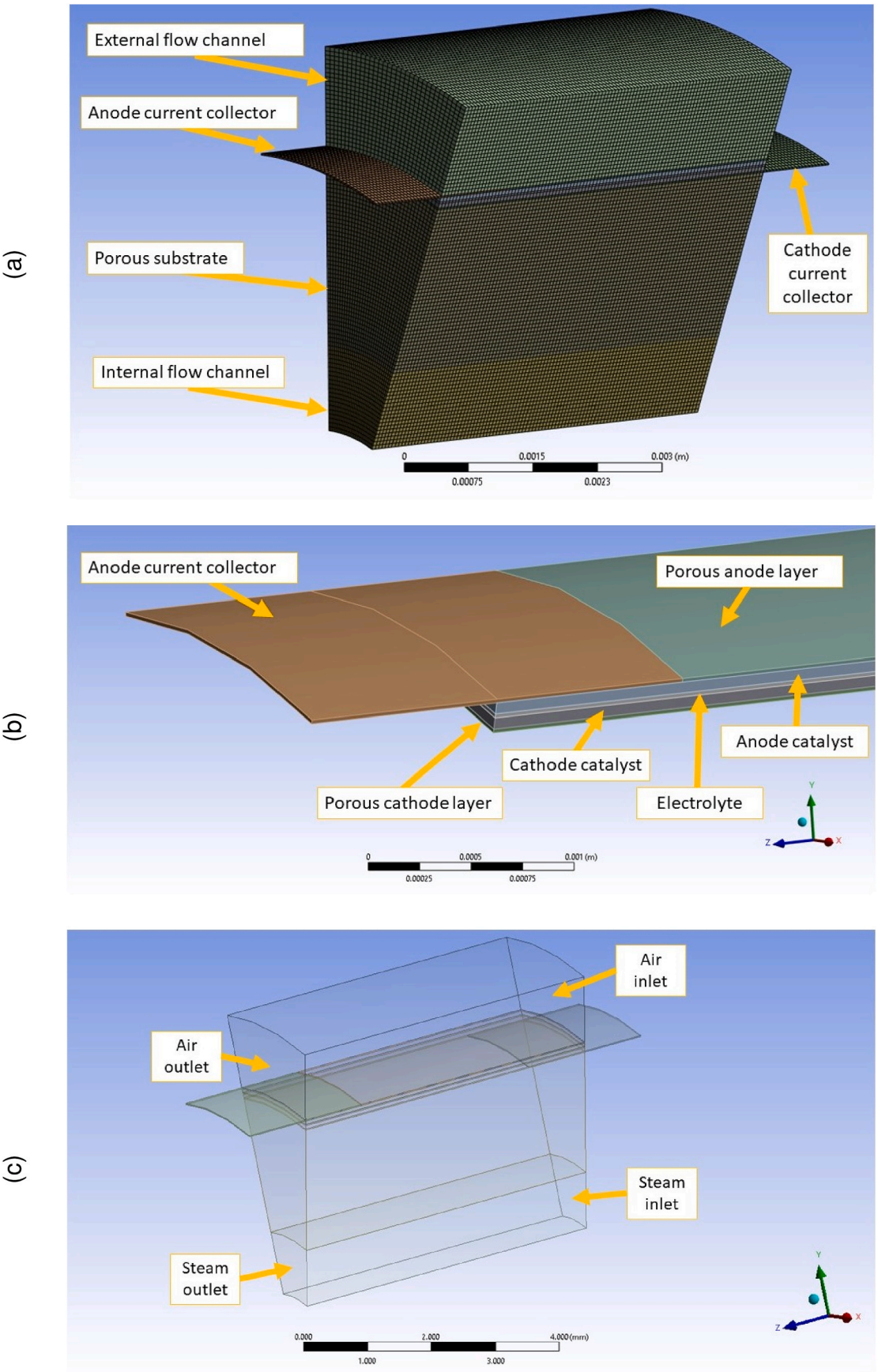

Fig. 1. General view of the SOEC sector model: (a) full meshed model of the tubular cell sector; (b) breakdown of the thin functional layers; (c) inlet and outlet boundary conditions.

Table 1
Characteristic sizes and layers' properties.

Structure	Internal diameter, mm	Wall thickness, mm	Materials	Volume proportion	Design porosity, %
Substrate	6.00	2.15	Ti	100 %	30
Cathode current collector	10.30	0.02	Ag	100 %	30
Porous cathode	10.30	0.02	NiO, GDC	60 %:40 %	30
Cathode	10.34	0.06	NiO, GDC	60 %:40 %	30
Electrolyte	10.46	0.022	GDC, YSZ	91 %:9 %	30
Anode	10.504	0.06	GDC, LSCF	50 %:50 %	30
Porous anode	10.624	0.02	GDC, LSCF	50 %:50 %	30
Anode current collector	10.624	0.02	Ag	100 %	30

Table 2
Material properties.

Material composition of the layer	Density, kg/m^3	Specific heat, J/(kg*K)	Thermal conductivity, W/(m*K)	Electrical conductivity calculated/Referenced, S/m
Titanium	4850	544	7	2381000
Silver	10490	235	429	6300000
Nickel	6670	445	91	25000
LSCF	6000	340	58	6
YSZ	5900	620	2	2
GDC	7200	216	11	99

2.3. Benchmarking with SOFC

To ensure the accuracy of the developed model, benchmarking is carried out using established reference data. Building on the previous studies (e.g., Ref. [64–66]), benchmarking of the numerical method in the current investigation is performed using the data from Ref. [67] for the tubular SOFC model (as appears in Fig. 2). Obtained results are shown in Fig. 3 below for the voltage range of 0.66–0.76 V. In the work by Ref. [67], the fuel cell of 130 mm length is studied, with the 40 μm thick electrolyte layer and the internal channel diameter of 4 mm. The benchmarking study is performed assuming the cell temperature of 973 K at 1 atmospheric pressure, 20 % proportion of hydrogen and 80 % proportion of water at the fuel inlet. The current study adopts the flow rates in the range of 1.11e-4 to 2.50e-4 kg/s for the air and 5.56e-7 to 2.22e-6 for the fuel (through two fuel channels), as proposed by Ref. [67], based on the utilization factors in Hagiwara et al. (1999) [68]. The SOFC module in ANSYS Fluent requires definition of the porous

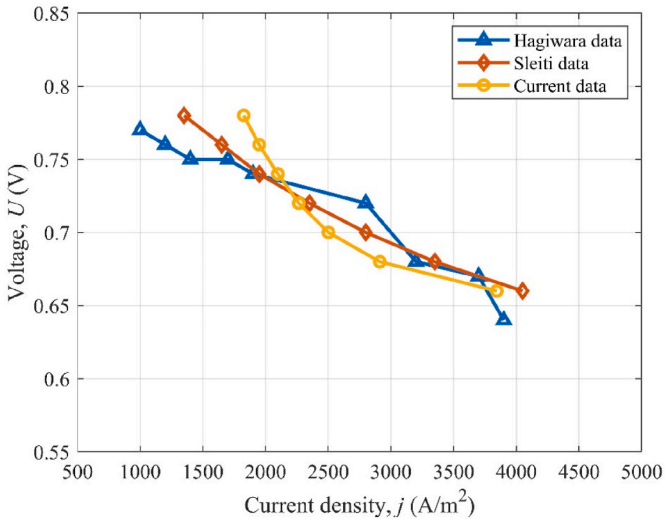

Fig. 3. Benchmarking with SOFC: Comparison of the current simulations with published simulation data by Ref. [67] and experimental data by Hagiwara et al. (1999) [68].

Table 3
Final material properties for the functional layers.

Material composition of the layer	Proportion of materials	Density, kg/m^3	Specific heat, J/(kg*K)	Thermal conductivity, W/(m*K)	Electrical conductivity calculated/Referenced, S/m	Default suggested electrical conductivity, S/m	Function of the layer
NiO, GDC	60 %:40 %	6882	353	59	15040	5000	Cathode
GDC, YSZ	91 %:9 %	7083	252	10	91	1e-16	Electrolyte
GDC, LSCF	50 %:50 %	6600	278	35	53	5000	Anode

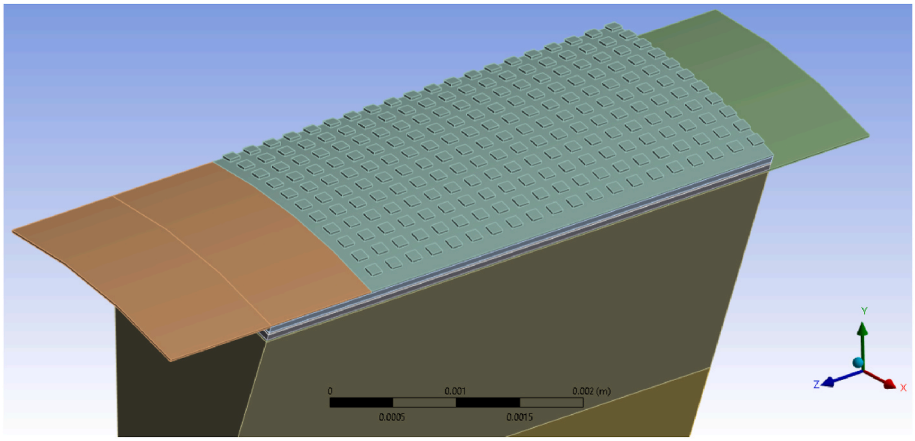

Fig. 2. SOEC model with the metasurface deposited on the porous anode layer (without the air channel).

electrode in addition to the catalyst layer for both anode and cathode sides, so that in the present research, the proportion of 90:10 of the catalyst thickness to the porous electrode thickness is used to obtain the SOFC results. Therefore, the cell design considered includes porous cathode, cathode, electrolyte, anode and porous anode. This may be one of the reasons to some observed discrepancy in the results in Fig. 3. Another reason is likely linked to the exact material properties of the LSCF, GDC, cermet and the dense ceramics used to manufacture the SOFC, according to Ref. [67]. The current study uses properties in Table 4. Results in Fig. 3 are also obtained on the grid of 648 000 elements, based on the mesh independence study for 0.7 V and the mass flow rates of 1.8e-4 kg/s for the air and 1.39 kg/s for the fuel, as presented in Table 5.

The current study uses SIMPLE algorithm with the least squares cell-based method for the gradient for the steady-state benchmarking simulations. Second order schemes are used for the pressure, density, momentum, species and energy, while first order schemes are selected for potentials, water saturation and content. Advanced solution controls use Flexible cycle type for the pressure and momentum, water saturation and content, and F-cycles with BCGSTAB method – for the energy, species and potentials. Selection is based on minimised residuals, which are set at 1e-4 for the simulation.

2.4. Mesh verification of the SOEC sector model

The main mesh independence study is conducted on the SOEC sector model without the metasurface and with the focus on the current density, as indicated in Fig. 4. The mesh size was determined through mesh independence tests, ensuring that further refinement would not significantly affect the accuracy of the results. The selected mesh resolution aligns with previous studies in similar computational domains. Based on this investigation, the mesh of 1 837 632 cells is selected, with the main size of the element of 5e-5 m, and 1.2e-5 m element size assigned to the functional layers. All metasurface cases, discussed in the next section, have the same mesh generation settings, so that processes in the thin functional layers are resolved with a comparable accuracy.

Here and in all simulations presented in the following section, advanced solution controls use V-cycle for pressure, F-cycle for energy and Flexible cycle for all other variables, based on the minimised residuals. Other solution settings are the same as used in the benchmarking case in Subsection 2.3 of the paper.

3. Results and discussion

Four types of metasurface elements considered in this study are shown in Fig. 5 and include square-shaped elements, line-elements and net structure. The net structure is comprised of parallel- and cross-flow line-elements. Some details of these geometrical configurations are given in Table 6 along with the principal current density for the operating voltage of 1.5 V, OCV of 1.1 V for comparison. These results of the CFD analysis indicate that the Metasurface 1 (small squares) leads to 3.7 % improvement in the current density, compared for the no-metasurface (base case). Here, width of the squared element (in the direction of circumference), length (in the direction of the flow/length of the cell), offsets (distances in between the elements in the direction of width and length) are assumed to be 0.1 mm, the elements' height is 0.05 mm.

Table 4
Material properties used in the benchmarking study.

Zone	Density, kg/m^3	Specific heat, J/kg*K	Thermal conductivity, W/m*K	Electrical conductivity, S/m
Porous anode	6000	871	10	33333
Anode catalyst	6000	871	10	33333
Electrolyte	6000	600	5	1e-16
Cathode catalyst	7200	871	10	7937
Porous cathode	6210	871	10	7937

Table 5
Mesh independence study for 0.7 V.

Mesh number	Cell count	Element size, m	Current density, A/m^2
Mesh 1	93 852	0.00055	6679
Mesh 2	213 516	0.00040	5579
Mesh 3	609 356	0.00027	3707
Mesh 4	648 000	0.00026	2463
Mesh 5	713 440	0.00025	2953
Mesh 6	928 806	0.00023	2576

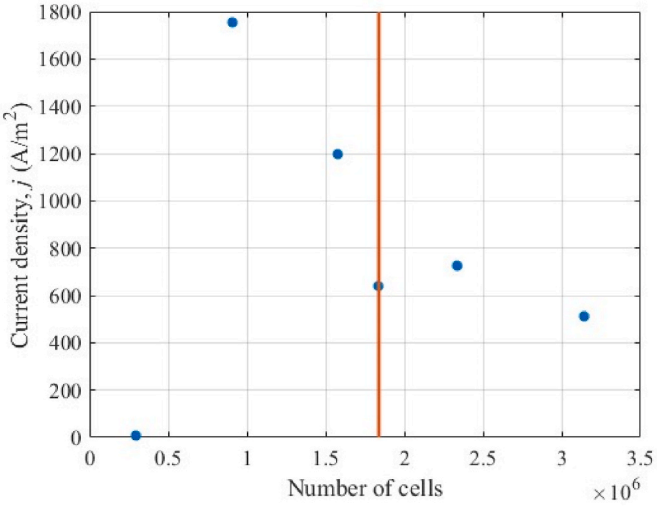

Fig. 4. Mesh independence test results for the base case without the metasurface.

Very similar, 4.2 % improvement in the current density is demonstrated by the Metasurface 4 (with twice large squares). Here, the width/length/offsets of 0.2 mm and the height of 0.05 mm of the square-shaped elements is used. The Metasurface 2 (lines, parallel to the flow) with line-elements of the width/distance between the elements of 0.1 mm and height of 0.05 mm in Fig. 5 and Table 6 provides the 7.6 % improvement in the current density. Finally, application of the net structure in the Metasurface 3 in Table 6, with line-elements of 0.1 mm in width/distance between the elements leads to 8.5 % improvement in the current density.

Following these results, Fig. 6 provides the view on the meshed porous anode layer with the four metasurfaces applied. Fig. 7(a) demonstrates the current density metrics for the range of voltage from 1.2 V to 2.0 V (high voltage typically considered to drive the steam reduction reaction efficiently) for five types of surfaces, starting with the plain porous anode without the metasurface. Here, the net-structured metasurface confirms its' advantageous current density characteristics over the full range of the considered operating voltage, given the 1.1 V OCV. This is likely linked to the recirculation (encouraging the air to swirl or loop around within those voids, rather than simply passing through) of the air flow in the pockets of space between the net structure elements.

The air circulation in the external air channel, where fluid is in a direct contact with the anode, is presented in Fig. 7(b)–7(f) for the case without a metasurface at 1.5 V voltage. The pressure and velocity fields here are projected on a plane slicing the channel at 10° deep into the 22.5° sector model (close to the midsection of the sector). Fig. 7(b) demonstrates a gradual decrease in the pressure in the air channel along the length of the cell, which comes together with the gradual increase in

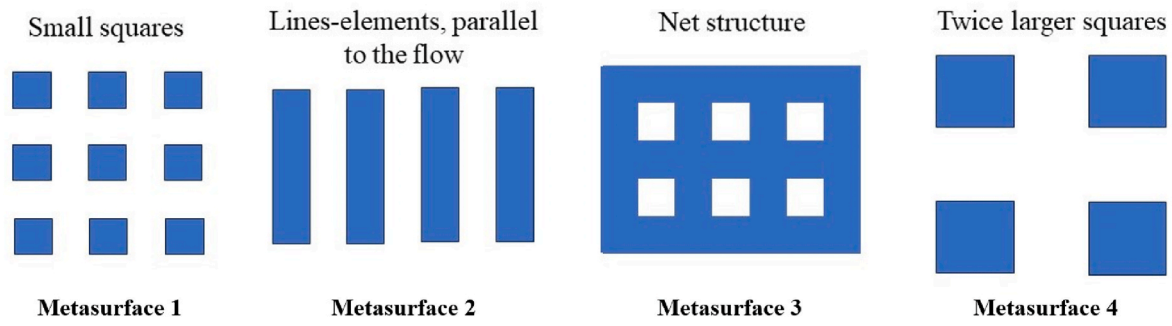

Fig. 5. Schematics of four considered metasurface design.

Table 6
Metasurface characteristics.

#	Metasurface types	No. of metasurface elements	No. of mesh cells	No. of iterations	Current density[a], A/m^2	Current density[b], A/m^2	Current density[c], A/m^2
0	Without metasurface (Base case)	0	1 837 632	1000	641	647	476
1	Small squares	11 × 20 square elements	5 028 880	200	665	668	492
2	Lines, parallel to the flow	11 line-elements	5 558 873	200	690	691	510
3	Net structure	11 × 20 line-elements	5 938 371	200	696	698	512
4	Large squares	5.5 × 10 square elements	4 636 929	200	668	670	493

[a] At 1.5V operating voltage & the OCV of 1.1 V.
[b] At 1.8V operating voltage & the OCV of 1.4 V.
[c] At 1.1V operating voltage & the OCV of 0.84 V.

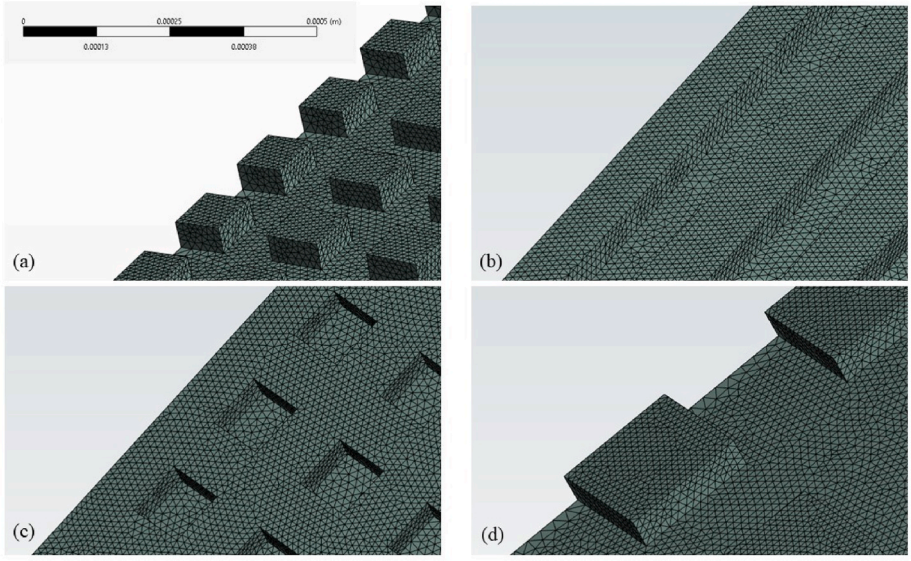

Fig. 6. Meshed porous anode layer with metasurfaces: (a) small squares; (b) line-elements, parallel to the air flow; (c) net structure; (d) twice large squares.

the flow velocity $U = U(u,v,w)$ along the centreline towards the outlet in Fig. 7(c). The air inlet is on the right side of each plot in Figs. 7 and 8. The velocity field U is dominated by the w velocity component, shown in Fig. 7(f), which leads to almost straight, smooth streamlines in Fig. 7(c). Two zones of increased positive and negative flow velocity u and v are observed in Fig. 7(d) and **(e)** respectively near the inlet, however, these local velocity fluctuations have a small effect on the downstream flow field.

This air circulation in the external gas channel is presented in detail in Fig. 8 for the same slicing plane, but for the net-structured metasurface. Fig. 8(b) illustrates the generally decreasing pressure in the air channel towards the place of transition from the metasurface level to the current collector, but not towards the outlet (as previously seen in the no-metasurface case). This decrease in pressure develops alongside the increase in the overall flow velocity U near the border of the anode metasurface in Fig. 8(f), which is a porous medium filled with fluid in contact with the solid body of the anode current collector. This localised increase in the flow velocity stimulates the formation of two major vortices of air circulation between the channel wall and the metasurface layer, as seen in Fig. 8(a) and (e). These vortices coincide with two elongated zones of decreased flow velocity U in Fig. 8(f). Formation of these major vortices is the first distinctive effect of all metasurfaces on the circulation in the air channel, as seen from Figs. 7 and 8 (additional results provided in the Supplementary Material).

Using the velocity components u, v, w in X, Y, Z directions, the process of major vortex formation and smaller scale recirculation in the

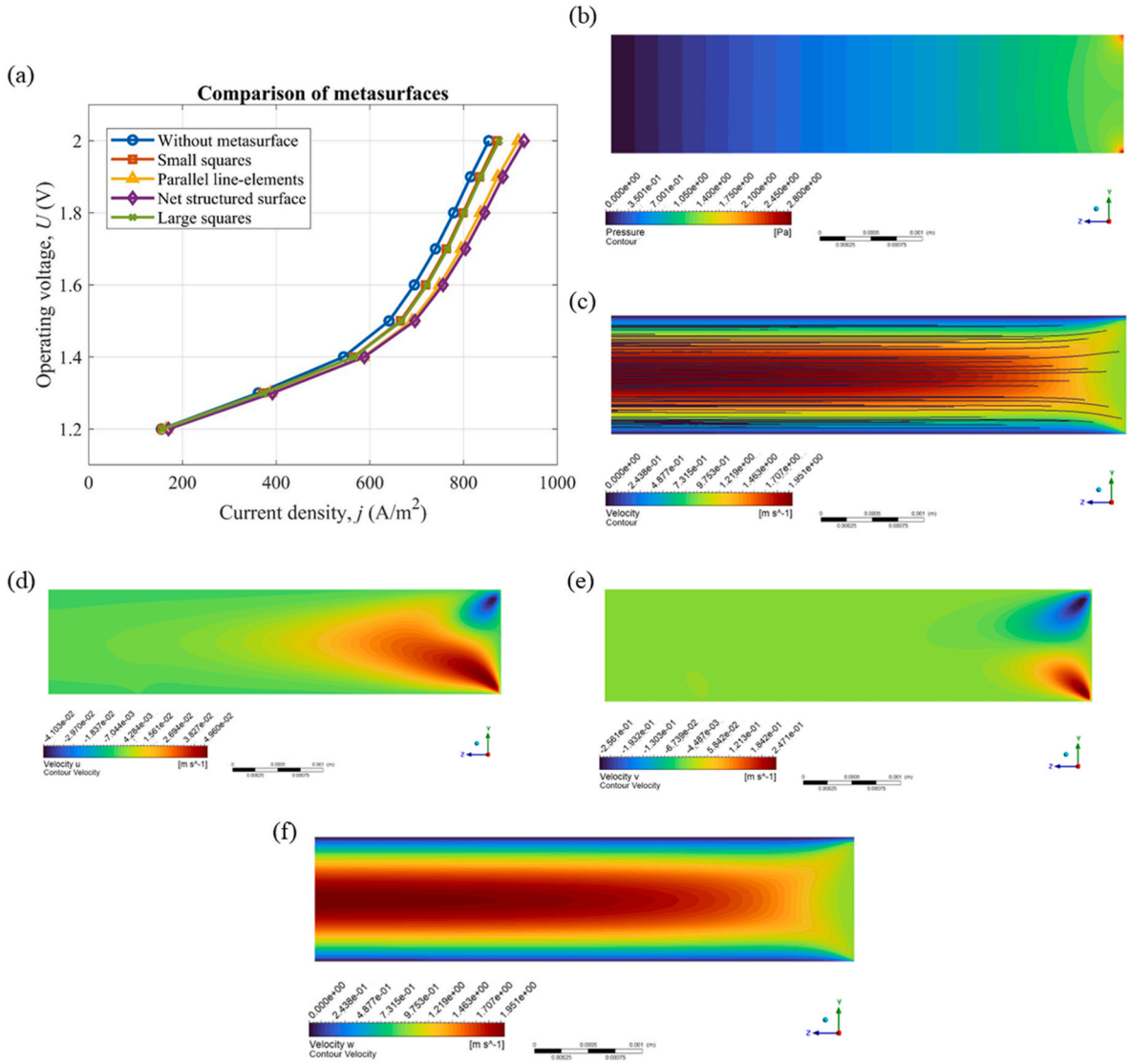

Fig. 7. Characterisation of cases: (a) current density – voltage characteristics of five types of considered surfaces; (b) pressure contour of the air channel at 10° for the no-metasurface case; (c) surface streamlines and velocity *U(u,v,w)* contour of the air channel at 10° for the no-metasurface case; (d) velocity *u* contour of the air channel at 10° for the no-metasurface case; (e) velocity *v* contour of the air channel at 10° for the no-metasurface case; (f) velocity *w* contour of the air channel at 10° for the no-metasurface case.

metasurface caves of the net structure could be further broken down in details. Fig. 8(g) indicates a localised increase in the velocity *u*, transversal to the length of the cell, in the first quarter of the length of the cell from the inlet boundary, followed by the vortex core and the area where fluid moves in the opposite direction. Zones of increased positive and negative velocity *u* also repeat further downstream, near the transition from the metasurface layer to the anode current collector. Fig. 8(i) reveals the localised increases in the velocity *v*, where the air flow accelerates up and down, especially around each vortex eye. Contour of the velocity component *w* in Fig. 8(k) is relatively consistent with the contour of the resulting velocity *U*, indicating the dominance of this longitudinal velocity component.

Fig. 8(l) further explains a gradual decrease of the longitudinal velocity *w* in the caves of the net-structured metasurface. This decrease develops together with relatively average values of the transversal velocity *u* and vertical velocity *v* in Fig. 8(h) and **(j),** respectively. Interaction of the air flow with the metasurface also leads to a local small-scale decrease in the pressure field past each metasurface element, as shown in Fig. 8(d), followed by an increase in pressure closer to the edge of each next metasurface element. These pressure fluctuations are consistent with the local fluctuations of the vertical velocity *v* in Fig. 8 (j), marking the fluid coming in and out of each cave. Separated fluid further circulates inside each cave, as illustrated in Fig. 8(c) with local streamlines.

According to the results for all metasurface cases, the improved electrical efficiency is, first of all, directly linked to the major vortices developing in the external air channel. Research into the fluid dynamics, developed in the air channel with line-elements metasurface, reveals patterns in the velocity *U* field, like the net-structured and square-shaped metasurfaces. In the presence of longitudinal caves only, the electrical efficiency of parallel line-elements alone is coming from the couple of major vortices in the air channel and does not rely on the small-scale recirculation. Based on this observation, the success of the net-structured metasurface is explained by harvesting the full efficiency of major vortices (like line-elements), and an additional efficiency is coming from the small-scale recirculation in the anode caves (like square elements). For the square elements, as provided in the *Supplementary Material,* the cave recirculation process along the length of the cell is observed to be weaker, and the surface in contact with the major vortices is lower, which may explain their comparatively reduced

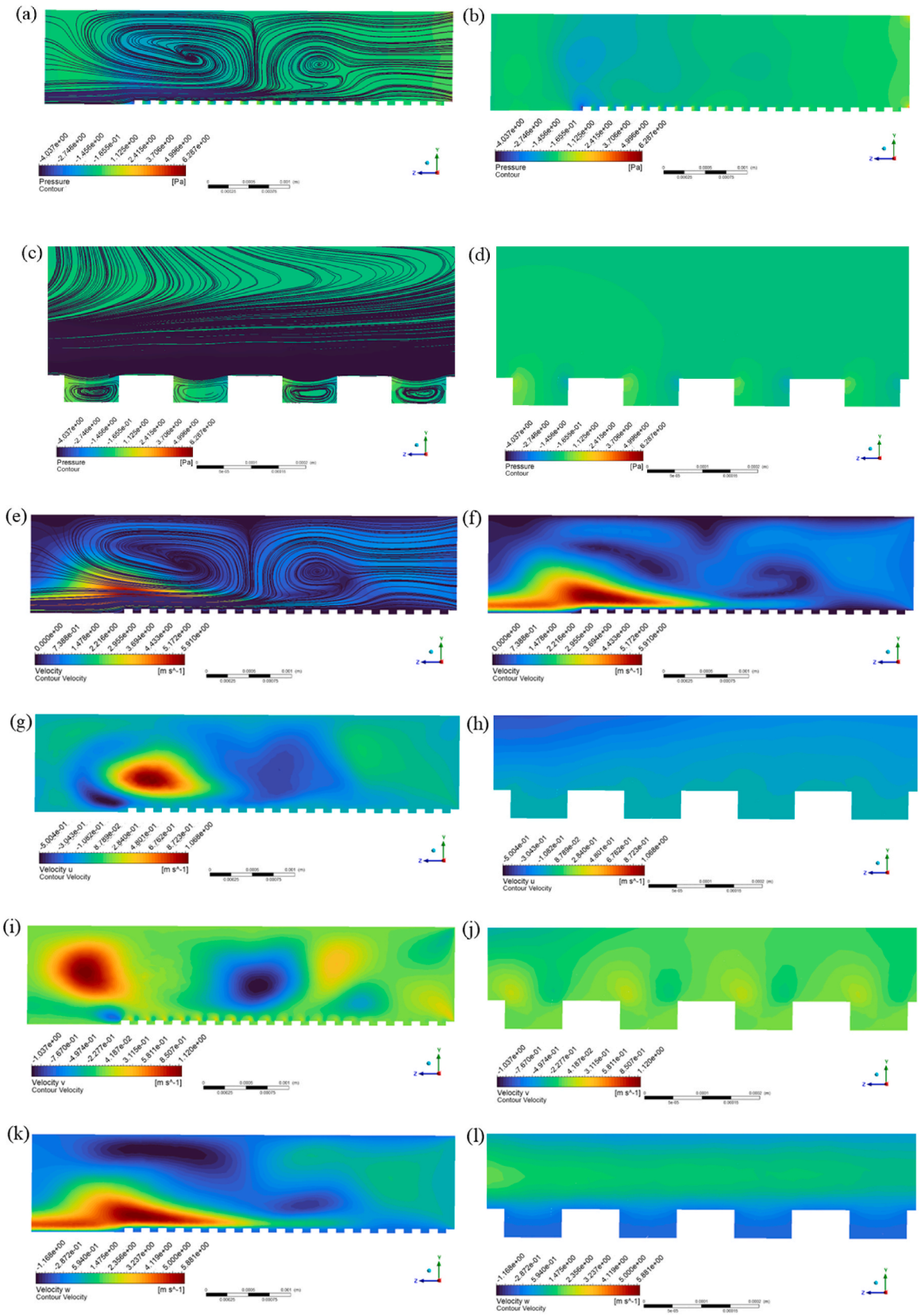

Fig. 8. Contours of the air circulation in the external channel for the case of net-structured metasurface, projected on the plane at 10° inclination inside the tubular cell sector: (a) full view on the air circulation streamlines over the pressure contour of the air channel; (b) full pressure contour of the air channel; (c) enlarged view on the air circulation streamlines over the pressure contour of the air channel in proximity to metasurface; (d) pressure contour in proximity to the metasurface; e) streamlines of the air circulation over the full velocity *U* contour of the air channel; (f) full velocity *U* contour of the air channel; (g) full contour of velocity component *u*; (h) enlarged contour of velocity component *u* in proximity to the metasurface; (i) full contour of velocity component *v*; (j) enlarged contour of velocity component *v* in proximity to the metasurface; (k) full contour of velocity component *w*; (l) enlarged contour of velocity component *w* in proximity to the metasurface.

electrical efficiency in Fig. 7(a).

4. Opportunities

The fundamental electrochemical and thermodynamic principles governing SOFC and SOEC operations are inherently linked. Many studies in the field successfully use SOFC-mode calibration to predict SOEC performance with high accuracy. The model's parameter adjustments account for reversible electrochemical reactions, ensuring its applicability across both operational modes. The model was initially calibrated in SOFC mode, and comparative analysis with published data reinforces the model's accuracy. The predictions align with experimental trends from SOEC studies, confirming its validity. The study acknowledges variations and provides a rational explanation for any differences, considering factors such as operating conditions, material properties, and measurement uncertainties. Refinements or additional calibration steps can be implemented in future work. While further refinement with direct SOEC-mode calibration can enhance precision, the current model provides a valuable predictive tool for SOEC performance analysis.

The best performance curve is found to belong to the net structure, among the studied options, with up to 8.5 % improvement compared to the case without the metasurface. Use of metamaterials for solid oxide electrolysers opens a space of opportunities for improving the device performance by the geometry optimisation. First opportunity comes from using various regular elements deposited on the porous anode layer or porous cathode layer, for either tubular or planar SOEC: metasurface elements of a different cross-section (squared, rectangular, round, triangular, hexagonal, etc.), tandem elements vs. staggered elements, equally spaced elements vs. non-evenly spaced elements, elements of varying height, length or width across the metasurface, or other type of a metasurface pattern. In many engineering and materials science applications, even modest performance gains can result in substantial long-term benefits, especially when considering scalability, energy efficiency, and operational stability. The study provides measured gains that reinforce the feasibility of metasurface structures in practical applications.

Consideration of the conical and cylindrical pillars have already been explored in Ref. [62]. This work studied both the fuel cell and electrolysis modes of operation for the 3D-structured metasurface design, with three functional layers of the cathode, electrolyte and anode being patterned, while deposited upon a porous substrate. Designed solid pillars had a height of up to 150 μm (against 50 μm in the present study) and diameter up to 50 μm (against the 100 μm side of the square in the present work for the first metasurface). This research also considered porous pillars of up to 190 μm height and up to 30 μm in diameter. This study reported the 1.14 times increase in the level of the current density in the electrolysis mode, and 1.93 times increase – in the fuel cell mode. The present work expands the available research data on the impact of metasurfaces on the electrical performance in terms of the current density towards alternative design patterns (squares, line-elements, net structure).

The second, related, opportunity is in introducing a flexible degree of irregularity in the metasurfaced layer, such as randomization of the characteristic element sizes and inter-element distances across the surface. Irregular shape of the element could come together with a different density of elements per unit surface area and/or a randomized height, which has a great potential to alter the fluid-structure interaction and the electrochemistry of the selected layer.

Several challenges also come from introducing the micro-functionality of the metasurface in SOECs. The first challenge of deposition of thin metasurface layers has been discussed in Ref. [58], where precision of the geometry of separate elements is found to require additional improvement. Introducing custom geometries, including increasing irregularity among the meta-elements would require fabricating custom-made precise meshes for the material deposition. Hence, the manufacturing costs are likely to increase, as the regular, available meshes cannot be used in the process.

Another challenge comes from the high-temperature operating conditions, where electrodes and thin coatings are already known to expand, degrade, debond, delaminate and crack. Structural stability is one of the design priorities for SOECs, and introduction of complex shapes for either layer changes the short-term and long-term degradation scenarios. This question requires additional research for each design concept.

5. Conclusions

The current research is undertaken in the pursuit of improving the performance of the tubular solid oxide electrolysis cell, operating at a high temperature of 1073 K. The study considers parallel flow conditions, and the porous anode layer in contact with the air flow is equipped with the metasurface of several various configurations. Metasurface elements change the fluid-structure interaction and intensity of electrochemical reactions, by increasing the surface area in contact with the air. Line-elements parallel to the length of the tubular cell, net structure and square-shaped metasurface elements are designed to be compared in terms of the current density characteristics. The best performance curve is found to belong to the net structure, among the studied options, with up to 8.5 % improvement compared to the case without the metasurface.

This design can be recommended for the practical implementation in the tubular and planar SOEC. Metasurface elements applied for solid oxide electrolysers open a new design space of potential cell improvements. By optimising current density, the metasurface may allow for the creation of smaller, more efficient devices with greater functionality. Opportunities come with several challenges, especially linked to possible irregularities in the meta-elements' geometry, which require a custom fabrication process. However, the potential gain in the micro-scale functionality, confirmed by the present work, and innovations in the rapidly developing additive manufacturing technology are likely to overcome these challenges in the future. The metasurface innovation is one of the promising changes to the SOEC, which could allow the technology to eventually mature and become an important part of the sustainable energy sector.

CRediT authorship contribution statement

Victoria Kurushina: Writing – original draft, Visualization, Validation, Software, Methodology, Investigation, Formal analysis, Data curation, Conceptualization. **Mamdud Hossain:** Writing – review & editing, Supervision, Methodology, Investigation, Funding acquisition, Formal analysis. **Syafawati Hasbi:** Methodology. **Ajith Soman:** Writing – review & editing. **Anil Prathuru:** Writing – review & editing, Supervision, Methodology, Investigation, Funding acquisition. **Qiong Cai:** Writing – review & editing, Supervision, Funding acquisition. **Bahman Amini Horri:** Writing – review & editing, Supervision, Funding acquisition. **Nadimul Haque Faisal:** Writing – review & editing, Supervision, Project administration, Methodology, Investigation, Funding acquisition, Formal analysis, Data curation, Conceptualization.

Declaration of competing interest

The authors declare that they have no known competing financial interests or personal relationships that could have appeared to influence the work reported in this paper.

Acknowledgements

The authors acknowledge high temperature steam electrolysis related funding by the UKRI EPSRC via Grants No. EP/W033178/1 (METASIS). VK would like to acknowledge the support of the National Project "Science and Universities" of the Ministry of Science and Higher

Education of the Russian Federation, grant number FEWN-2024-0005.

Appendix A. Supplementary data

Supplementary data to this article can be found online at https://doi.org/10.1016/j.jpowsour.2025.237436.

Data availability

Data will be made available on request.

References

[1] C.M. Stoots, J.E. O'Brien, K.G. Condie, J.J. Hartvigsen, High-temperature electrolysis for large-scale hydrogen production from nuclear energy–experimental investigations, Int. J. Hydrogen Energy 35 (10) (2010) 4861–4870, https://doi.org/10.1016/j.ijhydene.2009.10.045.

[2] V. Kurushina, V. Rajendran, A. Prathuru, M. Hossain, A. Soman, B. Horri, Q. Cai, N. Faisal, Thermomechanical deformation analysis of a tubular solid oxide steam electrolysis cell, in: https://tfaws.nasa.gov/tfaws23/proceedings/, 2023.

[3] J. Udagawa, P. Aguiar, N. Brandon, Hydrogen production through steam electrolysis: control strategies for a cathode-supported intermediate temperature solid oxide electrolysis cell, J. Power Sources 180 (1) (2008) 354–364, https://doi.org/10.1016/j.jpowsour.2008.01.069.

[4] O. Schmidt, A. Gambhir, I. Staffell, A. Hawkes, J. Nelson, S. Few, Future cost and performance of water electrolysis: an expert elicitation study, Int. J. Hydrogen Energy 42 (52) (2017) 30470–30492, https://doi.org/10.1016/j.ijhydene.2017.10.045.

[5] M.F. Ruth, Technoeconomic Analysis of Nuclear-Renewable Hybrid Energy Systems-Opportunities, Learnings, and Challenges, National Renewable Energy Lab.(NREL), Golden, CO (United States), 2019. https://www.osti.gov/biblio/1571753.

[6] D.C. Bingaman, M.K. Holly, J.L. Mace, C. Rice, R.K. Agarwal, M.K. Bradley, W. Smith, U. Bhattarai, Syste. Eng. Appro. Transition Zero Emission Avia. 3516 (2022), https://doi.org/10.2514/6.2022-3516.

[7] V.R. Larson, S.A. Evans, Propulsion for the space station, Acta Astronaut. 16 (1987) 379–389, https://doi.org/10.1016/0094-5765(87)90126-3.

[8] M. Hwang, T.-S. Rho, H.J. Lee, Conceptual design and performance analysis of water electrolysis propulsion system with catalytic igniter for CubeSats, Acta Astronaut. 200 (2022) 316–328, https://doi.org/10.1016/j.actaastro.2022.08.022.

[9] M. Rostami, M.D. Manshadi, A.H. Farajollahi, M. Marefati, Introducing and evaluation of a new propulsion system composed of solid oxide fuel cell and downstream cycles; usage in unmanned aerial vehicles, Int. J. Hydrogen Energy 47 (28) (2022) 13693–13709, https://doi.org/10.1016/j.ijhydene.2022.02.104.

[10] U. Gotzig, M. Wurdak, N. Harmansa, Development and coupled thruster/electrolyser tests of a water propulsion system, Acta Astronaut. 202 (2023) 751–759, https://doi.org/10.1016/j.actaastro.2022.09.059.

[11] F.E. Meyen, M.H. Hecht, J.A. Hoffman, MOXIE Team, Thermodynamic model of Mars oxygen ISRU experiment (MOXIE), Acta Astronaut. 129 (2016) 82–87, https://doi.org/10.1016/j.actaastro.2016.06.005.

[12] D.W. Harris, P.D. Kessler, T.M. Nickens, A.J. Choate, B.L. Horvath, M.A. Simon, C. Stromgren, Moon to Mars (M2M) habitation considerations: a snap shot as of January 2022. https://ntrs.nasa.gov/api/citations/20220000524/downloads/M2M%20Habitation%20Considerations%20TM%20-%20Final.pdf, 2022.

[13] J.B. McClean, J.A. Hoffman, M.H. Hecht, A.M. Aboobaker, K.R. Araghi, S. Elangovan, C.R. Graves, J.J. Hartvigsen, E.D. Hinterman, A.M. Liu, Pre-landing plans for mars oxygen in-situ resource utilization experiment (MOXIE) science operations, Acta Astronaut. 192 (2022) 301–313, https://doi.org/10.1016/j.actaastro.2021.12.003.

[14] K.E. Goodliff, N.F. Merancy, S.S. Bhakta, M.A. Rucker, P.R.-P. Chai, T.E. Ashurst, P. A. Troutman, C. Stromgren, Exploration Systems Development Mission Directorate (ESDMD) moon-to-mars Architecture Definition Document, National Aeronautics and Space Administration, 2023. https://ntrs.nasa.gov/api/citations/20230002706/downloads/M2MADD_ESDMD-001(TP-20230002706. pdf.

[15] A. Choate, D. Harris, T. Nickens, P. Kessler, M. Simon, NASA's Moon to Mars (M2M) Transit Habitat Refinement Point of Departure Design, IEEE Aerospace Confere. 1–18 (2023), https://doi.org/10.1109/AERO55745.2023.10115552.

[16] J.A. Hoffman, E.R. Hinterman, M.H. Hecht, D. Rapp, J.J. Hartvigsen, 18 months of MOXIE (Mars oxygen ISRU experiment) operations on the surface of mars-preparing for human Mars exploration, Acta Astronaut. (2023), https://doi.org/10.1016/j.actaastro.2023.04.045.

[17] Department for Business, Energy and Industrial Strategy, Net zero strategy. https://www.gov.uk/government/publications/net-zero-strategy, 2021.

[18] J. Jiang, R. Zhou, H. Xu, H. Wang, P. Wu, Z. Wang, J. Li, Optimal sizing, operation strategy and case study of a grid-connected solid oxide fuel cell microgrid, Appl. Energy 307 (2022) 118214, https://doi.org/10.1016/j.apenergy.2021.118214.

[19] S. Jiang, H. Suo, T. Zhang, C. Liao, Y. Wang, Q. Zhao, W. Lai, Recent advances in seawater electrolysis, Catalysts 12 (2) (2022) 123, https://doi.org/10.3390/catal12020123.

[20] Z. Jiang, A.L. Snowdon, A. Siddiq, A. El-Kharouf, R. Steinberger-Wilckens, Optimization of a ScCeSZ/GDC bi-layer electrolyte fabrication process for intermediate temperature solid oxide fuel cells, Ceram. Int. 48 (22) (2022) 32844–32852, https://doi.org/10.1016/j.ceramint.2022.07.211.

[21] C. Harman, L. Loch, C. Austin, Special Report on Properties of Solid Oxides for NEPA Project, 808, United States Atomic Energy Commission, 1948.

[22] E. Winter, 239. Studies of the exchange reactions of solid oxides. Part I. The exchange of oxygen isotopes between gaseous oxygen and certain metallic oxides, J. Chem. Soc. (1950) 1170–1175. https://pubs.rsc.org/en/content/articlelanding/1950/jr/jr9500001170/unauth.

[23] J. Miles, P. Smith, The formation of metal oxide films using gaseous and solid electrolytes, J. Electrochem. Soc. 110 (12) (1963) 1240, https://doi.org/10.1149/1.2425633.

[24] H. Spacil, C. Tedmon, Electrochemical dissociation of water vapor in solid oxide electrolyte cells: II. Materials, fabrication, and properties, J. Electrochem. Soc. 116 (12) (1969) 1627, https://doi.org/10.1149/1.2411643.

[25] T. Etsell, S.N. Flengas, Electrical properties of solid oxide electrolytes, Chem. Rev. 70 (3) (1970) 339–376. https://pubs.acs.org/doi/pdf/10.1021/cr60265a003?casa_token=SWX4oC4pUUcAAAAA:0HyqVGpkOpCzv8aw54ntnmdbIrYOi1eaE5MDxvSid131WsIe64XAznz2UzzlSSu2amXeICUTJBXTOwI.

[26] C. Alcock, S. Zador, Electrolytic removal of oxygen from gases by means of solid electrolyte, J. Appl. Electrochem. 2 (4) (1972) 289–299, https://doi.org/10.1007/BF00615276.

[27] H. Tuller, A. Nowick, Doped ceria as a solid oxide electrolyte, J. Electrochem. Soc. 122 (2) (1975) 255, https://doi.org/10.1149/1.2134190.

[28] W. Doenitz, R. Schmidberger, E. Steinheil, Perspectives and problems of high temperature electrolysis of water vapour using solid oxide electrolytes, 1978, in: https://www.google.co.uk/books/edition/Proceedings_of_the_Symposium_on_Industri/_FufAAAAIAAJ?hl=en&gbpv=0.

[29] P. Lu, S. Srinivasan, Advances in water electrolysis technology with emphasis on use of the solid polymer electrolyte, J. Appl. Electrochem. 9 (3) (1979) 269–283, https://doi.org/10.1007/BF01112480.

[30] W. Doenitz, R. Schmidberger, E. Steinheil, R. Streicher, Hydrogen production by high temperature electrolysis of water vapour, Int. J. Hydrogen Energy 5 (1) (1980) 55–63, https://doi.org/10.1016/0360-3199(80)90114-7.

[31] S. Inami, C. Mc Cullough, S. Ring, W. Smart, J. Weissbart, Development of a carbon dioxide-water solid oxide electrolyte electrolysis system annual report, 29 Mar. 1968-29 May 1969, https://ntrs.nasa.gov/api/citations/19690024930/downloads/19690024930.pdf, 1969.

[32] W. Smart, J. Weissbart, Development of a CO2-H2O solid oxide electrolysis system annual report, 1 Apr.-31 Dec. 1970, https://ntrs.nasa.gov/api/citations/19710013696/downloads/19710013696.pdf, 1970.

[33] A.O. Isenberg, R.J. Cusick, Carbon dioxide electrolysis with solid oxide electrolyte cells for oxygen recovery in life support systems, SAE Trans. (1988) 360–373. https://www.jstor.org/stable/44470334.

[34] T.M. Maloney, Computer Modeling of Solid Oxide Fuel Cells, Cleveland State University, 1990. https://www.proquest.com/openview/cf837d46edcfbb1b6ca0b3df89617ab3/1?pq-origsite=gscholar&cbl=18750&diss=y.

[35] J. Mizusaki, K. Amano, S. Yamauchi, K. Fueki, Electrode reaction at Pt, O2 (g)/stabilized zirconia interfaces. Part I: theoretical consideration of reaction model, Solid State Ionics 22 (4) (1987) 313–322, https://doi.org/10.1016/0167-2738(87)90149-4.

[36] J. Kupecki, L. Mastropasqua, K. Motylinski, D. Ferrero, Multilevel modeling of solid oxide electrolysis, in: Solid Oxide-based Electrochemical Devices, Elsevier, 2020, pp. 123–166, https://doi.org/10.1016/B978-0-12-818285-7.00005-8.

[37] A. Banerjee, Y. Wang, J. Diercks, O. Deutschmann, Hierarchical modeling of solid oxide cells and stacks producing syngas via H2O/CO2 Co-electrolysis for industrial applications, Appl. Energy 230 (2018) 996–1013, https://doi.org/10.1016/j.apenergy.2018.08.122.

[38] Z. Li, H. Zhang, H. Xu, J. Xuan, Advancing the multiscale understanding on solid oxide electrolysis cells via modelling approaches: a review, Renew. Sustain. Energy Rev. 141 (2021) 110863, https://doi.org/10.1016/j.rser.2021.110863.

[39] L. Wehrle, D. Schmider, J. Dailly, A. Banerjee, O. Deutschmann, Benchmarking solid oxide electrolysis cell-stacks for industrial power-to-methane systems via hierarchical multi-scale modelling, Appl. Energy 317 (2022) 119143, https://doi.org/10.1016/j.apenergy.2022.119143.

[40] A.C. Ince, M.F. Serincan, C.O. Colpan, U. Pasaogullari, A mini review on mathematical modeling of co-electrolysis at cell, stack and system levels, Fuel Process. Technol. 244 (2023) 107724, https://doi.org/10.1016/j.fuproc.2023.107724.

[41] J.D. Duhn, A.D. Jensen, S. Wedel, C. Wix, Optimization of a new flow design for solid oxide cells using computational fluid dynamics modelling, J. Power Sources 336 (2016) 261–271, https://doi.org/10.1016/j.jpowsour.2016.10.060.

[42] X. Zhang, B. Liu, Y. Yang, J. Li, J. Li, Y. Zhao, L. Jia, Y. Sun, Advances in component and operation optimization of solid oxide electrolysis cell, Chin. Chem. Lett. 34 (5) (2022) 108035, https://doi.org/10.1016/j.cclet.2022.108035.

[43] Y. Xu, J. Zhang, Z. Tu, Numerical simulation of flow channel geometries optimization for the planar solid oxide electrolysis cell, Int. J. Hydrogen Energy 52 (Part B) (2023) 288–301, https://doi.org/10.1016/j.ijhydene.2023.07.242.

[44] T. Cui, J. Zhu, Z. Lyu, M. Han, K. Sun, Y. Liu, M. Ni, Efficiency analysis and operating condition optimization of solid oxide electrolysis system coupled with different external heat sources, Energy Convers. Manag. 279 (2023) 116727, https://doi.org/10.1016/j.enconman.2023.116727.

[45] M. Ni, Computational fluid dynamics modeling of a solid oxide electrolyzer cell for hydrogen production, Int. J. Hydrogen Energy 34 (18) (2009) 7795–7806, https://doi.org/10.1016/j.ijhydene.2009.07.080.

[46] Z. Liang, J. Wang, Y. Wang, M. Ni, M. Li, Transient characteristics of a solid oxide electrolysis cell under different voltage ramps: transport phenomena behind

overshoots, Energy Convers. Manag. 279 (2023) 116759, https://doi.org/10.1016/j.enconman.2023.116759.
[47] Y. Luo, Y. Shi, W. Li, N. Cai, Comprehensive modeling of tubular solid oxide electrolysis cell for co-electrolysis of steam and carbon dioxide, Energy (Calg.) 70 (2014) 420–434, https://doi.org/10.1016/j.energy.2014.04.019.
[48] X. Jin, X. Xue, Computational fluid dynamics analysis of solid oxide electrolysis cells with delaminations, Int. J. Hydrogen Energy 35 (14) (2010) 7321–7328, https://doi.org/10.1016/j.ijhydene.2010.04.158.
[49] M. Navasa, J. Yuan, B. Sundén, Computational fluid dynamics approach for performance evaluation of a solid oxide electrolysis cell for hydrogen production, Appl. Energy 137 (2015) 867–876, https://doi.org/10.1016/j.apenergy.2014.04.104.
[50] Z. Fu, Z. Wang, Y. Li, J. Li, Y. Shao, Q. Zhu, P. Weng, Effects of composite electrode structure on performance of intermediate-temperature solid oxide electrolysis cell, Energies 15 (19) (2022) 7173, https://doi.org/10.3390/en15197173.
[51] C. Kang, P. Huaiwu, Z. Junfeng, X. Xinxin, Z. Shengchen, R. Jingxin, L. Biao, W. Yueshe, Analysis of performance optimization of high-temperature solid oxide electrolytic cell based on the coupling of flow, heat, and mass transfer and electrochemistry, Energy Sci. Eng. 10 (10) (2022) 3918–3927, https://doi.org/10.1002/ese3.1255.
[52] C. Liu, Z. Dang, G. Xi, Numerical study on thermal stress of solid oxide electrolyzer cell with various flow configurations, Appl. Energy 353 (2024) 122041, https://doi.org/10.1016/j.apenergy.2023.122041.
[53] G. Hawkes, J. O'Brien, C. Stoots, B. Hawkes, 3D CFD model of a multi-cell high-temperature electrolysis stack, Int. J. Hydrogen Energy 34 (9) (2009) 4189–4197, https://doi.org/10.1016/j.ijhydene.2008.11.068.
[54] Q. Li, Y. Zheng, W. Guan, L. Jin, C. Xu, W.G. Wang, Achieving high-efficiency hydrogen production using planar solid-oxide electrolysis stacks, Int. J. Hydrogen Energy 39 (21) (2014) 10833–10842, https://doi.org/10.1016/j.ijhydene.2014.05.070.
[55] A.A. AlZahrani, I. Dincer, Thermodynamic and electrochemical analyses of a solid oxide electrolyzer for hydrogen production, Int. J. Hydrogen Energy 42 (33) (2017) 21404–21413, https://doi.org/10.1016/j.ijhydene.2017.03.186.
[56] D. González, L. Rojas, J. Rosales, L. Castro, A. Gámez, C. Brayner, L. García, C. García, R. de la Torre, D. Sánchez, Computational model for a high temperature electrolyzer coupled to a HTTR for efficient nuclear hydrogen production. https://inis.iaea.org/collection/NCLCollectionStore/_Public/47/006/47006417.pdf, 2015.
[57] P. Jiao, Mechanical energy metamaterials in interstellar travel, Prog. Mater. Sci. (2023) 101132, https://doi.org/10.1016/j.pmatsci.2023.101132.
[58] N.H. Faisal, N. Sellami, F. Venturi, T. Hussain, T. Mallick, F. Muhammad-Sukki, A. Bishop, H. Upadhyaya, N.K. Katiyar, S. Goel, Large-scale manufacturing route to metamaterial coatings using thermal spray techniques and their response to solar radiation, Emergent Mater. (2021) 1–15, https://doi.org/10.1007/s42247-021-00252-z.
[59] I. Jang, G. Kelsall, Fabrication of 3D NiO-YSZ structures for enhanced performance of solid oxide fuel cells and electrolysers, Electrochem. Commun. 137 (2022) 107260, https://doi.org/10.1016/j.elecom.2022.107260.
[60] N. Farandos, L. Kleiminger, T. Li, A. Hankin, G. Kelsall, Three-dimensional inkjet printed solid oxide electrochemical reactors. I. Yttria-stabilized zirconia electrolyte, Electrochim. Acta 213 (2016) 324–331, https://doi.org/10.1016/j.electacta.2016.07.103.
[61] S. Masciandaro, M. Torrell, P. Leone, A. Tarancón, Three-dimensional printed yttria-stabilized zirconia self-supported electrolytes for solid oxide fuel cell applications, J. Eur. Ceram. Soc. 39 (1) (2019) 9–16, https://doi.org/10.1016/j.jeurceramsoc.2017.11.033.
[62] I. Jang, J. Alexander, N. Farandos, G. Kelsall, Predicting optimal geometries of 3D-printed solid oxide electrochemical reactors, Electrochim. Acta 427 (2022) 140902, https://doi.org/10.1016/j.electacta.2022.140902.
[63] M. Navasa, Three dimensional multiphysics modeling of reversible solid oxide electrochemical cells for degradation studies. https://portal.research.lu.se/en/publications/three-dimensional-multiphysics-modeling-of-reversible-solid-oxide, 2016.
[64] Y. Cao, A solar-driven lumped SOFC/SOEC system for electricity and hydrogen production: 3E analyses and a comparison of different multi-objective optimization algorithms, J. Clean. Prod. 271 (2020) 122457, https://doi.org/10.1016/j.jclepro.2020.122457.
[65] A. Habibollahzade, E. Gholamian, A. Behzadi, Multi-objective optimization and comparative performance analysis of hybrid biomass-based solid oxide fuel cell/solid oxide electrolyzer cell/gas turbine using different gasification agents, Appl. Energy 233 (2019) 985–1002, https://doi.org/10.1016/j.apenergy.2018.10.075.
[66] M. Viviani, G. Canu, M.P. Carpanese, A. Barbucci, A. Sanson, E. Mercadelli, C. Nicolella, D. Vladikova, Z. Stoynov, A. Chesnaud, Dual cells with mixed protonic-anionic conductivity for reversible SOFC/SOEC operation, Energy Proc. 28 (2012) 182–189, https://doi.org/10.1016/j.egypro.2012.08.052.
[67] A.K. Sleiti, Performance of tubular solid oxide fuel cell at reduced temperature and cathode porosity, J. Power Sources 195 (17) (2010) 5719–5725, https://doi.org/10.1016/j.jpowsour.2010.03.044.
[68] A. Hagiwara, H. Michibata, A. Kimura, M.P. Jaszcar, G.W. Tomlins, Tubular solid oxide fuel cell life tests, Proceedings of the Third International Fuel Cell Conference (D2-4, 1999) 369.

Supplementary material

Modelling metasurface patterned anode for enhanced performance of solid oxide electrolyser

Victoria Kurushina[a,b,1], Mamdud Hossain[a,1], Syafawati Hasbi[a], Ajith Soman[c], Anil Prathuru[a], Qiong Cai[c], Bahman Amini Horri[c], Nadimul Haque Faisal[a,1]

[a] *School of Computing, Engineering and Technology, Robert Gordon University, Aberdeen, AB10 7GJ, UK*

[b] *Laboratory of Vibration & Hydrodynamics Modelling, Industrial University of Tyumen, Tyumen, 625 000, Russia*

[c] *Department of Chemical & Process Engineering, University of Surrey, Guildford, GU2 7XH, UK*

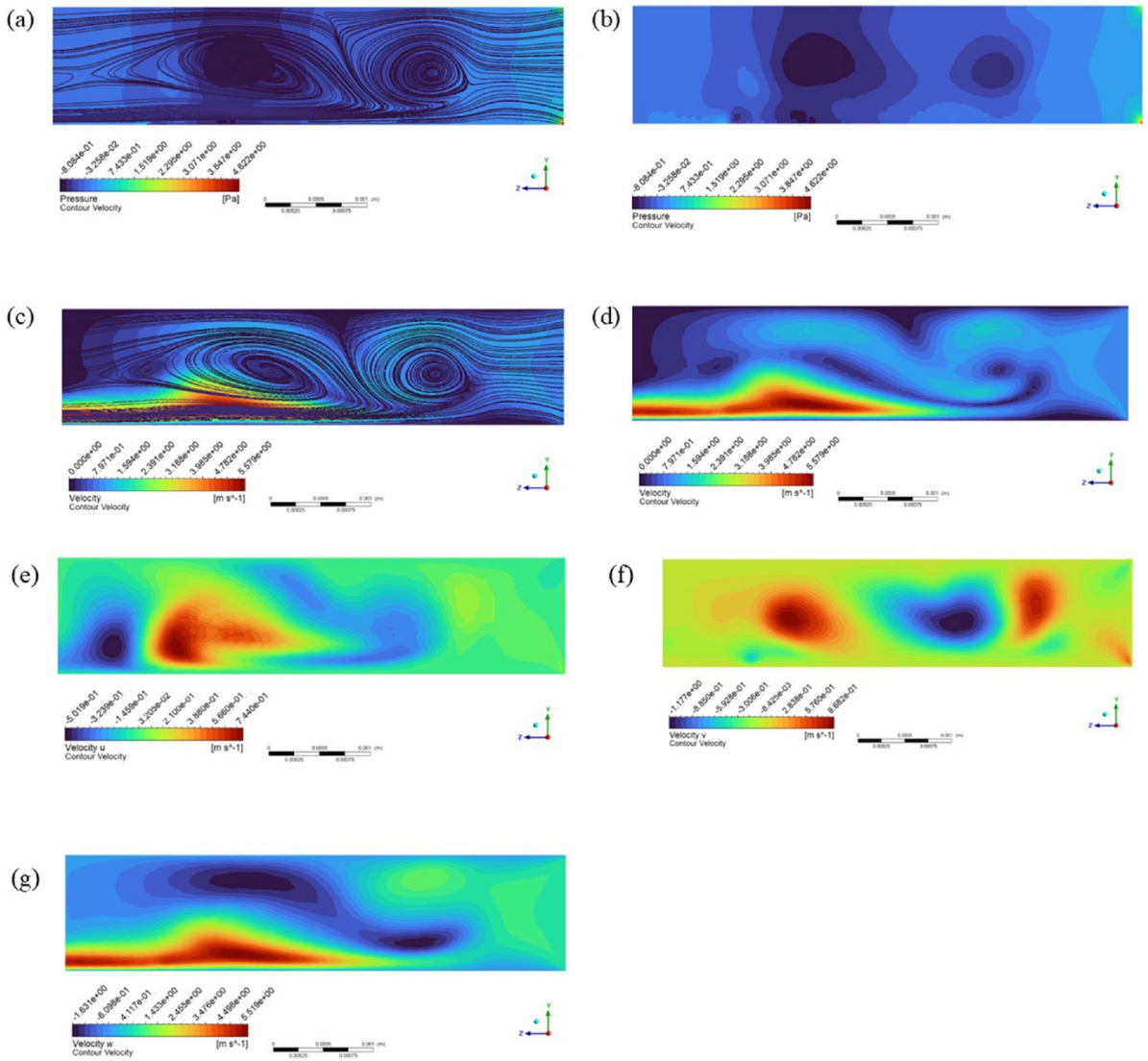

Fig. A. Contours of the air circulation in the external channel for the case of line-elements metasurface, projected on the plane at 10° inclination inside the tubular cell sector: (a) full view on the air circulation streamlines over the pressure contour of the air channel; (b) full pressure contour of the air channel; (c) streamlines of the air circulation over the full velocity *U* contour of the air channel; (d) full velocity *U* contour of the air channel; (e) full contour of velocity component *u*; (f) full contour of velocity component *v*; (g) full contour of velocity component *w*.

[1]Corresponding authors: v.kurushina@outlook.com; m.hossain@rgu.ac.uk; n.h.faisal@rgu.ac.uk

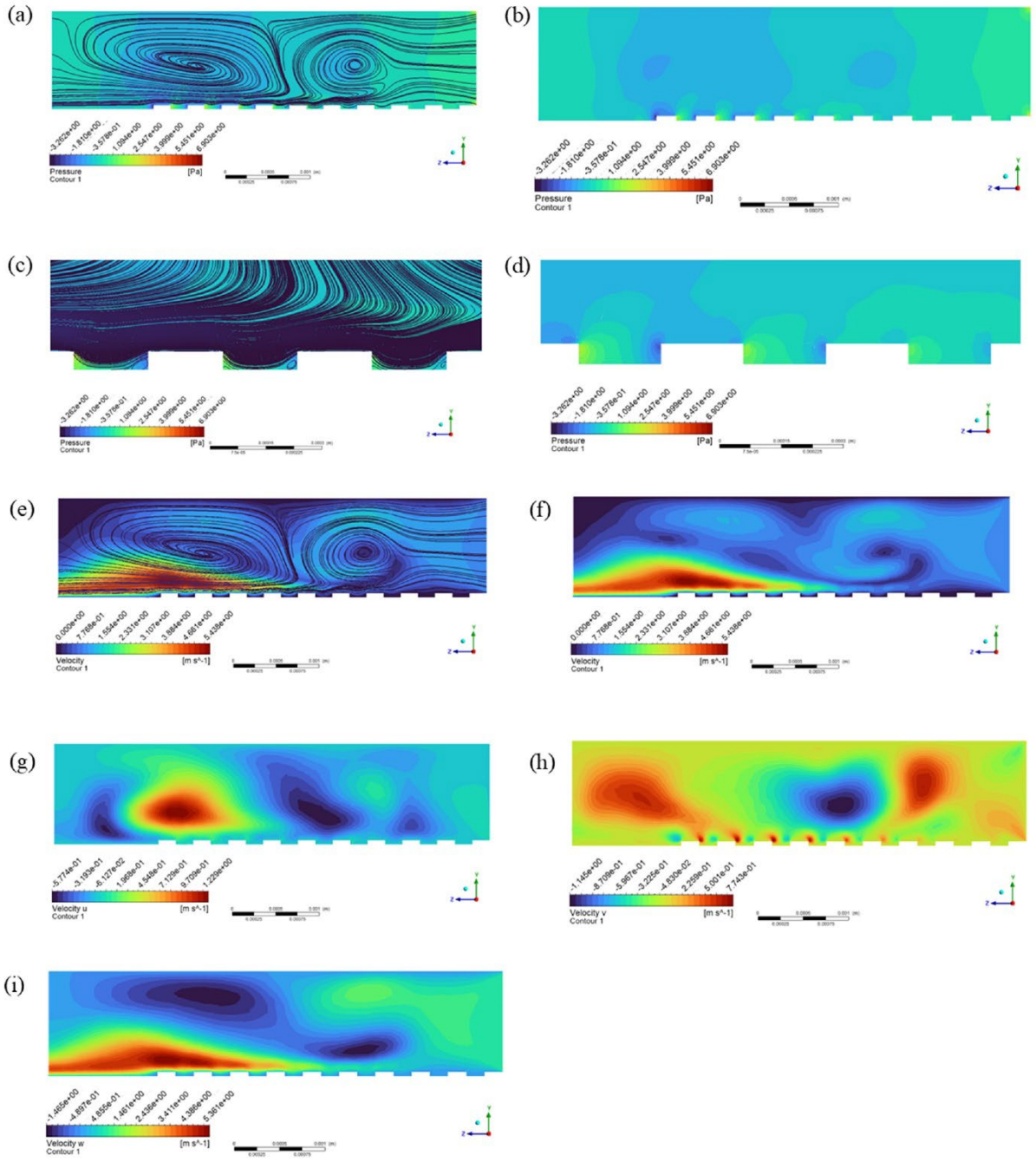

Fig. B. Contours of the air circulation in the external channel for the case of large-squares metasurface, projected on the plane at 10º inclination inside the tubular cell sector: (a) full view on the air circulation streamlines over the pressure contour of the air channel; (b) full pressure contour of the air channel; (c) enlarged view on the air circulation streamlines over the pressure contour of the air channel in proximity to metasurface; (d) pressure contour in proximity to the metasurface; e) streamlines of the air circulation over the full velocity *U* contour of the air channel; (f) full velocity *U* contour of the air channel; (g) full contour of velocity component *u*; (h) full contour of velocity component *v*; (i) full contour of velocity component *w*.